CrossMark

*J. Fluid Mech.* (2018), *vol.* 857, *pp.* 291–311. © Cambridge University Press 2018
doi:10.1017/jfm.2018.752



# Waves on a vortex: rays, rings and resonances

**Theo Torres[1,2,†], Antonin Coutant[1,2], Sam Dolan[3] and Silke Weinfurtner[1,2]**

[1]School of Mathematical Sciences, University of Nottingham, University Park, Nottingham NG7 2RD, UK

[2]Centre for the Mathematics and Theoretical Physics of Quantum Non-Equilibrium Systems, University of Nottingham, Nottingham NG7 2RD, UK

[3]Consortium for Fundamental Physics, School of Mathematics and Statistics, University of Sheffield, Hicks Building, Hounsfield Road, Sheffield S3 7RH, UK

(Received 19 January 2018; revised 10 September 2018; accepted 18 September 2018; first published online 22 October 2018)

We study the scattering of surface water waves with irrotational draining vortices. At small depth, this system is a mathematical analogue of a rotating black hole and can be used to mimic some of its peculiar phenomena. Using ray-tracing methods, we exhibit the existence of unstable orbits around vortices at arbitrary depth. These orbits are the analogue of the light rings of a black hole. We show that these orbits come in pairs, one co-rotating and one counter-rotating, at an orbital radius that varies with the frequency. We derived an explicit formula for this radius in the deep-water regime. Our method is validated by comparison with recent experimental data from a wavetank experiment. We finally argue that these rings will generate a discrete set of damped resonances that we characterize and that could possibly be observed in future experiments.

**Key words:** surface gravity waves, vortex flows, waves/free-surface flows

## 1. Introduction

The interaction between waves and vortices has attracted attention in various fields of physics (Vivanco *et al.* 2000), such as acoustics (Fetter 1964; Nazarenko, Zabusky & Scheidegger 1995; Pagneux & Maurel 2001; Kopiev & Belyaev 2010), ocean surface waves (Bühler & McIntyre 2005; Bühler 2014) and wave generation by turbulence (Lund & Rojas 1989; Cerda & Lund 1993; Fabrikant & Raevsky 1994; Umeki & Lund 1997). The problem was studied with the use of singularities in the complex plane by Vanden-Broeck & Keller (1987), Stokes, Hocking & Forbes (2008) and Moreira & Peregrine (2012). The stability analysis of rotating fluids is also a rich topic, in particular due to the possibility of 'over-reflection' mechanisms (Acheson 1976), which was studied both experimentally (Vatistas, Wang & Lin 1994; Jansson *et al.* 2006) and theoretically (Tophøj *et al.* 2013; Mougel *et al.* 2017).

The wave–vortex interaction is the setting for two intriguing physical analogies. Firstly, waves on a vortex give rise to a hydrodynamical analogue of the Aharonov–Bohm effect of quantum mechanics (Berry *et al.* 1980; Coste & Lund 1999; Coste,

† Email addresses for correspondence: theo.torresvicente@nottingham.ac.uk, antonin.coutant@ens-lyon.org, s.dolan@sheffield.ac.uk, Silke.Weinfurtner@nottingham.ac.uk

https://doi.org/10.1017/jfm.2018.752 Published online by Cambridge University Press

Lund & Umeki 1999; Vivanco *et al.* 1999; Sonin 2002; Dolan, Oliveira & Crispino 2011). Secondly, a draining vortex constitutes an (inexact) hydrodynamical analogue of a rotating black hole. Based on the original work of Unruh (1981), Schützhold & Unruh (2002) showed that (under reasonable physical assumptions) the propagation equation governing waves on a draining vortex is formally identical to that governing a massless scalar field on an 'effective' (but fictitious) black hole geometry. Further, the characteristics of the wave equation map onto the null geodesics (i.e. the light rays) of the black hole geometry. The presence of a horizon – a one-way membrane for rays and waves – leads to exotic wave phenomena such as superradiance (a particular case of over-reflection) or Hawking radiation (for reviews see e.g. Brito, Cardoso & Pani (2015) on superradiance, Jacobson (2013) on Hawking radiation and Barcelo, Liberati & Visser (2005) on analogue gravity). Analogous effects are expected in shallow fluid flows when the speed of the flow becomes comparable to the propagation speed of the waves.

Recently, there has been much interest in studying black hole analogue phenomenology in the laboratory. Amongst others, Weinfurtner *et al.* (2011), Euvé *et al.* (2016) and Steinhauer (2016) conducted laboratory-based experiments to mimic the analogue Hawking effect of a black hole. An analogue rotating black hole was exhibited in an optical system by Vocke *et al.* (2017). Torres *et al.* (2017) have reported the first observation of rotational superradiance, in a draining vortex. Notably, in this last experiment, the dispersive nature of the waves needs to be taken into account, and thus the effective-geometry description of Schützhold & Unruh (2002) is incomplete. Owing to a nonlinear dispersion relation, the phase and group velocities are not equal outside the shallow regime; quite unlike the case in relativity, where both are equal to the speed of light. Nevertheless, the key features predicted for the shallow-water, linear dispersion regime, such as superradiance and the Aharonov–Bohm effect, appear to be robust in real experiments, as observed by Berry *et al.* (1980) and Torres *et al.* (2017) for example.

A ubiquitous feature of a black hole is the existence of photon orbits called 'light rings'. Outside a Schwarzschild black hole, for example, there is a 'photon sphere', at $3/2$ times the event horizon radius, comprising the (zero-measure) set of light rays (null geodesics) that orbit around the black hole perpetually. These orbits comprise a separatrix in phase space, dividing between rays that fall into the black hole and rays that escape. Analysis of the properties of light rings yields a heuristic understanding of many black hole phenomena. The orbital frequency $\Omega$ and Lyapunov exponent $\Lambda$ of the light rings – just two parameters – play a dominant role in (semiclassical approximations to) the spectrum of damped resonances known as black hole quasi-normal modes (Goebel 1972; Cardoso *et al.* 2009; Dolan 2010; Yang *et al.* 2012; Konoplya & Stuchlík 2017), the absorption cross-section (Decanini, Esposito-Farese & Folacci 2011; Macedo *et al.* 2013) and wave-interference phenomena such as 'orbiting' and 'glories' in the scattering cross-section (Matzner *et al.* 1985; Dolan & Stratton 2017). For example, the frequency and decay rate of the 'ringdown phase' in gravitational wave chirp signals, such as GW150914 detected by Abbott *et al.* (2016), are determined by the black hole quasi-normal mode frequencies (Schutz & Will 1985; Berti, Cardoso & Starinets 2009).

A key aim of this paper is to show that there generically exist circular orbits around a draining vortex, which are the analogue of black hole light rings. To do so, we apply ray-tracing methods, well used in hydrodynamics, astronomy and elsewhere, to analyse perturbations of real fluid-mechanical systems, such as vortices, in which dispersion and/or dissipation play a significant role. In § 3, we apply the methods to show that

https://doi.org/10.1017/jfm.2018.752 Published online by Cambridge University Press

scattering of waves in a draining vortex can be well understood in terms of the rays of a frequency-dependent effective Hamiltonian, and we obtain a transport equation for the wave amplitude. In § 4 we discuss the presence of circular orbits, and in § 5 discuss its consequences in terms of resonance appearing in the time-dependent response of the system.

## 2. Surface waves on a flow

We consider surface waves propagating on a flow of constant depth $h_0$. The flow is assumed incompressible ($\rho = \text{const.}$) and irrotational, so that the velocity flow is derived from a potential $\boldsymbol{v} = \boldsymbol{\nabla}\Phi$. On top of a background (mean) flow $\boldsymbol{v}_0 = \boldsymbol{\nabla}\Phi_0$, small perturbations $\phi = \Phi - \Phi_0$ propagate according to the wave equation (Milewski & Keller 1996)

$$\mathcal{D}_t^2\phi - \mathrm{i}(g\boldsymbol{\nabla} - \gamma\boldsymbol{\nabla}^3)\tanh(-\mathrm{i}h_0\boldsymbol{\nabla})\phi + 2\nu\boldsymbol{\nabla}^2\mathcal{D}_t\phi = 0, \tag{2.1}$$

where $\mathcal{D}_t = \partial_t + \boldsymbol{v}_0\cdot\boldsymbol{\nabla}$ is the material derivative, $g$ is the gravitational acceleration, $\gamma$ is the ratio of surface tension and the fluid density, $\nu$ is the viscosity of the fluid, and i is the imaginary number such that $\mathrm{i}^2 = -1$. In this equation, we included the effect of bulk dissipation, governed by the last term, but other sources of dissipation are generally present (Hunt 1964; Przadka *et al.* 2012; Robertson & Rousseaux 2017). To keep the discussion general, we introduce a pair of functions, $F$ and $\Gamma$, encoding the dispersion relation and dissipation, in order to write the wave equation in the following form:

$$\mathcal{D}_t^2\phi + F(-\mathrm{i}\boldsymbol{\nabla})\phi - 2\nu\Gamma(-\mathrm{i}\boldsymbol{\nabla})\mathcal{D}_t\phi = 0. \tag{2.2}$$

In the absence of background flow, solutions of (2.1) are given by plane waves $\phi = \mathrm{Re}[A\exp(-\mathrm{i}\omega t + \mathrm{i}\boldsymbol{k}\cdot\boldsymbol{x})]$ of amplitude $A$, angular frequency $\omega$ and wavevector $\boldsymbol{k}$ (of norm $k = \|\boldsymbol{k}\|$). Then $\omega$ and $\boldsymbol{k}$ obey the dispersion relation

$$\omega^2 = F(\boldsymbol{k}) - 2\mathrm{i}\nu\omega\Gamma(\boldsymbol{k}), \tag{2.3}$$

with the functions

$$F(\boldsymbol{k}) = (gk + \gamma k^3)\tanh(h_0 k) \quad \text{and} \quad \Gamma(k) = k^2. \tag{2.4a,b}$$

Note that the method we shall present stays identical for general functions $F$ and $\Gamma$, the only necessary assumptions being that they are analytic and even. In the absence of background flow, a wave packet propagates at a group velocity $\boldsymbol{v}_g$ given by

$$\boldsymbol{v}_g \doteq \boldsymbol{\nabla}_k\omega = \boldsymbol{\nabla}_k\sqrt{F}. \tag{2.5}$$

In the presence of a constant flow, one must distinguish between two notions of (angular) frequency: the intrinsic (fluid-frame) frequency $\Omega$ and the laboratory frequency $\omega$. The intrinsic frequency is the one satisfying the dispersion relation, while the laboratory one is conserved due to stationarity. The two are related by a Doppler shift: $\Omega = \omega - \boldsymbol{v}_0\cdot\boldsymbol{k}$. As a result, the group velocity in the laboratory frame is defined as

$$\boldsymbol{v}_g^{lab} = \boldsymbol{\nabla}_k\omega, \tag{2.6}$$

and obtained from the group velocity in the fluid frame using

$$\boldsymbol{v}_g^{f} \doteq \boldsymbol{\nabla}_k\sqrt{F} = \boldsymbol{v}_g^{lab} - \boldsymbol{v}_0. \tag{2.7}$$

Now when the background flow varies spatially, solutions of the wave equation become much more involved. This is why we shall now solve (2.1) using a ray-tracing method, to characterize the propagation of waves around vortices.

https://doi.org/10.1017/jfm.2018.752 Published online by Cambridge University Press

## 3. Ray-tracing equations

We shall now solve (2.1) using a gradient expansion – a common method in wave physics (see e.g. Bühler 2014). This means that we assume that the background flow changes over a scale significantly larger than the wavelength. To materialize this, a convenient procedure is to rescale the derivatives in (2.1) as $\partial \to \epsilon\partial$, and solve the equation perturbatively in $\epsilon$. We then look for wave solutions with a rapidly varying phase and a slowly varying amplitude, that is, we seek solutions of the form

$$\phi = A(\boldsymbol{x}) \exp\left(\mathrm{i}\frac{S(\boldsymbol{x})}{\epsilon}\right), \tag{3.1}$$

where $A$ is the local amplitude and $S$ is the local phase, both real-valued functions (of course, ultimately, one should take the real part of (3.1) to obtain the velocity potential fluctuation field). We now expand $S$ and $A$ in powers of $\epsilon$, and obtain an equation for the phase and one for the amplitude (in appendix A, we detail how to obtain them). At leading order in $\epsilon$, the phase $S_0$ obeys the Hamilton–Jacobi equation,

$$(\partial_t S_0 + \boldsymbol{v}_0 \cdot \boldsymbol{\nabla} S_0)^2 - F(\boldsymbol{\nabla} S_0) = 0. \tag{3.2}$$

This first-order partial differential equation can be solved by the method of (bi)characteristics. The characteristics are the rays of the waves. Substituting the $\boldsymbol{\nabla} S_0$ by the wavevector $\boldsymbol{k}$ and $\partial_t S_0$ by $-\omega$, we obtain the Hamiltonian of our system,

$$\mathcal{H} = -\tfrac{1}{2}(\omega - \boldsymbol{v}_0 \cdot \boldsymbol{k})^2 + \tfrac{1}{2}F(\boldsymbol{k}). \tag{3.3}$$

The characteristics are now obtained through Hamilton's equations:

$$\dot{t} = -\frac{\partial \mathcal{H}}{\partial \omega}, \quad \dot{\omega} = \frac{\partial \mathcal{H}}{\partial t}, \tag{3.4a}$$

$$\dot{x}_j = \frac{\partial \mathcal{H}}{\partial k_j} \quad \text{and} \quad \dot{k}_j = -\frac{\partial \mathcal{H}}{\partial x_j}, \tag{3.4b}$$

where the dot denotes the derivative with respect to a parameter $\lambda$, used to parametrize the rays, and the index $j$ is short for $(x, y)$. (The unusual sign in (3.4*a*) is due to the fact that the conjugate variable to $t$ is $-\omega$ and not $\omega$.) In addition to Hamilton's equations, one must ensure that the Hamiltonian constraint,

$$\mathcal{H} = 0, \tag{3.5}$$

is satisfied for all solutions. A satisfying feature of this constrained Hamiltonian formalism is that it is independent of the choice of parameter. One can multiply the Hamiltonian $\mathcal{H}$ by any non-vanishing function $N(\lambda)$, and one will find the same set of rays, instead parametrized by $\tilde{\lambda}$, where

$$\mathrm{d}\tilde{\lambda} = N(\lambda)\,\mathrm{d}\lambda. \tag{3.6}$$

The next-to-leading-order expansion of (2.1) in $\epsilon$ gives us the equation for the amplitude. This takes the form of a transport equation,

$$\partial_t(\Omega_0 A_0^2) + \boldsymbol{\nabla} \cdot (\Omega_0 A_0^2 \boldsymbol{v}_g^{lab}) = -2\nu\Omega_0 A_0^2 \gamma(\boldsymbol{\nabla} S_0). \tag{3.7}$$

https://doi.org/10.1017/jfm.2018.752 Published online by Cambridge University Press

Note that this equation can be solved once one has a solution $S_0$ of the Hamilton–Jacobi equation (3.2). In particular, the group velocity in (3.7) is a function of only the position: $\boldsymbol{v}_g(\boldsymbol{x}, p) \to \boldsymbol{v}_g(\boldsymbol{x}, \boldsymbol{\nabla} S_0(\boldsymbol{x}))$. The quantity $A_0^2\Omega_0$ is in fact the wave action (Bühler 2014), up to a factor of $\rho/g$. This equation implies that the wave action is moving with the velocity $\boldsymbol{v}_g^{lab}$. The dissipative term simply encodes the loss of wave action carried along the propagation. Since dissipation does not affect the equations (3.4) that determine the paths of the rays, we neglect it in the following.

Notice that we have so far considered a constant surface height. However, it is formally simple to add a varying height $h_0(x, y)$ at the level of Hamilton's equations (3.4). Such replacement will be valid if the variations of the surface height are slow enough. By this we mean, first, that the relative variations of the height are small $|\boldsymbol{\nabla} h_0| \ll 1$, so that its gradient can be neglected in the derivation of the wave equation (2.1); and, second, that the wavelength is small compared to the variation scale $|\boldsymbol{\nabla} h_0/(kh_0)|$, so that the eikonal approximation stays valid. In the experiment of § 4.2.1, the assumption of constant height is well satisfied outside a small radius near the centre, and hence we shall assume it in the rest of the paper.

## 4. Rays around a vortex

We shall now apply the ray-tracing equations to study the propagation of waves around a vortex. For this we consider the simplest model of an irrotational vortex with a drain. This model assumes that the surface is flat, and that the flow is homogeneous in the vertical direction and symmetric around the vertical axis. Under these assumptions, the irrotational and incompressibility conditions give us the profile

$$\boldsymbol{v}_0 = -\frac{D}{r}\boldsymbol{e}_r + \frac{C}{r}\boldsymbol{e}_\theta, \tag{4.1}$$

written in polar coordinates $(r, \theta)$ (see figure 1), and where $C$ and $D$ are the circulation and draining constants (positive), respectively. The schematic of the flow and the coordinate systems are presented in figure 1. This model is not only simple to analyse, it also provides a realistic description of a wide variety of situations. The reason is that, far from the centre (where the water depth drops), and far from the edges of the fluid tank (where circular symmetry breaks down), the free surface tends to be flat and the flow to resemble that of (4.1). As we will see, the effect we are after is contained in this region (see also figure 4 in Torres *et al.* (2017)). This model also corresponds (in the shallow-water regime) to a water-wave analogue of a rotating black hole (Visser 1998; Schützhold & Unruh 2002).

### 4.1. *Circular orbits*

Although we shall have in mind the flow profile of (4.1), our results stay conceptually identical for a large class of flows. To see this, the following discussion is done using a general symmetric flow of the form

$$\boldsymbol{v}_0 = v_r(r)\boldsymbol{e}_r + v_\theta(r)\boldsymbol{e}_\theta. \tag{4.2}$$

Using the symmetry of the vortex flow, we first switch to polar coordinates. We build the conjugate variables as before, that is, $k_r = \partial_r S$ and $m = \partial_\theta S$. As we shall see, depending on the context, $m$ will be a real number (interpreted as an angular momentum) or an integer (interpreted as the azimuthal number of the wave). We also

https://doi.org/10.1017/jfm.2018.752 Published online by Cambridge University Press

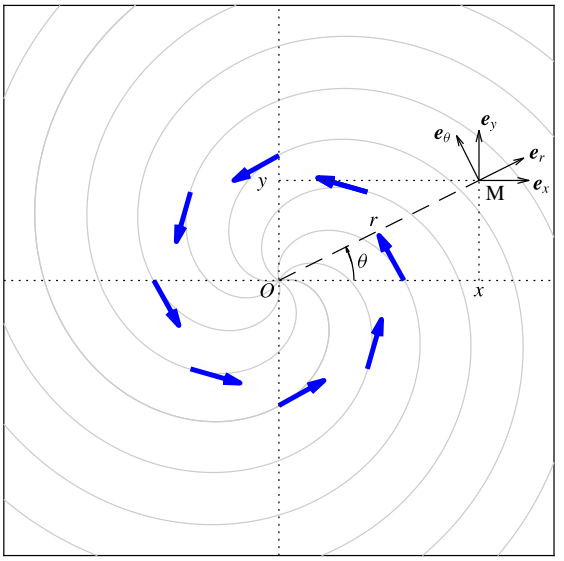



FIGURE 1. (Colour online) Schematic of the flow and associated coordinate systems, from the perspective of an observer looking down on the wavetank. The vortex considered here is rotating anticlockwise when $C > 0$ (as shown by the bold blue arrows). The light grey lines represent streamlines of the flow. A point M on the surface is located using either Cartesian coordinates $(x, y)$ or polar coordinates $(r, \theta)$.

note that $\omega$ is conserved since the flow is stationary. For simplicity, we assume $\omega > 0$ (but negative values can be obtained via the symmetry $\omega \to -\omega$ and $m \to -m$).

A circular orbit is an equilibrium point in the radial direction. This means that it is a critical point of the Hamiltonian for $(r, k_r)$. It thus satisfies the conditions

$$\partial_r \mathcal{H} = 0, \tag{4.3a}$$

$$\partial_{k_r} \mathcal{H} = 0. \tag{4.3b}$$

In the bathtub profile of (4.1), equations (4.3) give two relations between four unknowns. For a fixed pair $(\omega, m)$, equations (4.3) determine a unique pair $(r_\star, k_{r\star})$. Furthermore, imposing the Hamiltonian constraint $\mathcal{H} = 0$ gives a relation between $\omega$ and $m$ on the circular orbit, analogous to a dispersion relation, which we write as

$$\omega = \omega_\star(m). \tag{4.4}$$

This relation can be read in either of two ways: at fixed angular frequency $\omega$, it gives the value of $m$ such that one has a circular orbit; at fixed azimuthal number $m$, it yields the particular wave frequency corresponding to the circular orbit.

4.1.1. *Shallow-water regime*

In the limit of shallow water, where all modes propagate at the same speed, the radius of the circular orbit is independent of the angular frequency $\omega$, and furthermore the relationship between $\omega$ and $m$ is linear (see e.g. Dolan, Oliveira & Crispino 2012; Dempsey 2017):

$$\omega_\star = \hat{\Omega}^{\pm} m. \tag{4.5}$$

https://doi.org/10.1017/jfm.2018.752 Published online by Cambridge University Press

Here $\hat{\Omega}^{\pm} \equiv \dot{\theta}/\dot{t}$ is the orbital frequency of the circular orbit. In general, there exist two circular orbits, one co-rotating ($\dot{\theta} > 0$, $\hat{\Omega}^{+} > 0$) and one counter-rotating ($\dot{\theta} < 0$, $\hat{\Omega}^{-} < 0$) relative to the circulating flow. The frequencies are given by

$$\hat{\Omega}^{\pm} = \pm \frac{c^2\sqrt{C^2 + D^2}}{B_{\pm}^2}. \tag{4.6}$$

The radii of these circular orbits (which we shall now refer to as 'orbital radii') are then given by

$$r_{\star}^{\pm} = \frac{B_{\pm}}{c}, \tag{4.7}$$

where $c = \sqrt{gh}$ is the propagation speed of shallow-water waves, and a $+$ $(-)$ sign denotes the co-rotating (counter-rotating) case. The parameter $B_{\pm}$ is defined as

$$B_{\pm} = (2(C^2 + D^2) \mp 2C\sqrt{C^2 + D^2}\,)^{1/2}. \tag{4.8}$$

As we shall see, $B_{\pm}$ also governs the orbital radius for deep-water waves. An immediate conclusion of (4.7) is that the co-rotating circular orbit is closer to the centre of the vortex, while the counter-rotating orbit is further out. Hence, the counter-rotating orbit is in general more visible (this is further confirmed in § 5 when studying damped resonances).

4.1.2. *Deep-water regime*

For further insight into circular orbits in the presence of dispersion, it is instructive to look at another simple case where analytic formulae can be obtained. Here we consider deep water without capillarity, and thus a group velocity given by

$$v_g(k) = \frac{1}{2}\sqrt{\frac{g}{k}}. \tag{4.9}$$

In this regime it is possible to derive a simple formula for the radius of the orbits as a function of the frequency. We can directly express the norm of the wavevector in terms of the radius as

$$|\boldsymbol{k}| = \frac{g r_{\star}^2}{4B_{\pm}^2} \tag{4.10}$$

(with $\pm$ indices omitted on $k$ and $r_{\star}$ for clarity). With the other conditions for the circular orbits, equations (4.3), we can express both $k_{r\star}$ and $m$ as functions of $r_{\star}$, *viz.*,

$$k_{r\star} = \frac{D g r_{\star}^2}{4B_{\pm}^3} \quad \text{and} \quad m = \frac{g r_{\star}^3}{4B_{\pm}^2}\sqrt{1 - \frac{D^2}{B_{\pm}^2}}. \tag{4.11$a$,$b$}$$

Combining these expressions and using the Hamiltonian constraint, we obtain the radii of the unstable orbits as a function of the frequency and the effective dispersion relation (see appendix B for detail):

$$r_{\star} = \frac{8B_{\pm}}{3g}\omega_{\star} \tag{4.12}$$

https://doi.org/10.1017/jfm.2018.752 Published online by Cambridge University Press

and

$$\omega_\star(m) = \frac{3}{8}\left(\frac{4g^2}{\sqrt{B_\pm^2 - D^2}}\right)^{1/3} m^{1/3}. \tag{4.13}$$

Note that the wave angular frequency $\omega_\star$ scales linearly with $m$ in shallow water, but with $m^{1/3}$ in deep water. This is a direct consequence of the dispersive nature of the waves.

4.1.3. *General case*

For any nonlinear dispersion relation, equations (4.3) imply the relation

$$r_\star = \frac{B_\pm}{v_g^f}. \tag{4.14}$$

This equation shows that it is the change in the group velocity $v_g^f$ that shifts the location of the circular orbit. Here $v_g^f$ is evaluated with the local wavevector on the orbit $k^2 = k_{r\star}^2 + m^2/r_\star^2$, and hence the equation above is implicit. To find $r_\star$ and $\omega_\star(m)$ explicitly, one must insert (4.14) into (4.3) and the Hamiltonian constraint.

Figure 2 shows numerically obtained solutions for the orbital radius as a function of wave frequency, for a vortex with $C/hc = D/hc = 0.9$. The two branches correspond to the co-rotating (+) and counter-rotating (−) orbits. At low frequency (long wavelength), the orbital radius is anticipated by the shallow-water result, equation (4.5). At higher frequencies, the circular orbits migrate away from the vortex core, as anticipated in (4.12). Even though the ray structure will qualitatively be similar for various values of the parameters $C$ and $D$, one can distinguish two interesting limits. First, when $C \gg D$, we can see that the radius of the co-rotating orbit shrinks to zero as $B_+ \to 0$. In contrast, when $C \ll D$, the two circular orbits asymptotically approach one another as $B_+ \to B_-$.

At this level, it is instructive to discuss the case of a vortex without a drain. By taking the limit $D \to 0$ in (4.7) and (4.12), we see that the co-rotating orbit degenerates to $r = 0$, but the counter-rotating one still exists at a non-zero radius (e.g. $C/2c$ in the shallow-water regime). For sound waves, it was shown by Nazarenko (1994) and Nazarenko *et al.* (1995) that rays approaching $r = 0$ of an ideal non-draining vortex (equation (4.1) with $D = 0$) see their wavelength decrease to zero, and ultimately reach the dissipative scale. As such rays do not escape, it suggests that the scattering will be similar to a vortex with small drain (that is $D \neq 0$ but $D \ll C$). In particular, we expect to have a counter-rotating orbit, as well as the associated resonance effects (see § 5). (We thank an anonymous referee for having stimulated this discussion, and for pointing out references Nazarenko (1994) and Nazarenko *et al.* (1995).)

## 4.2. *Ray scattering*

We now study a family of characteristics (rays) encroaching upon the vortex from the right ($x \to +\infty$) with angular frequency $\omega$ and various impact parameters $b$, which is the ray equivalent of sending a plane wave. Here, $m$ is a continuous parameter that is given in terms of the impact parameter via the relation

$$b = \frac{m}{k_{in}} + \frac{C}{v_g^{in}}. \tag{4.15}$$

https://doi.org/10.1017/jfm.2018.752 Published online by Cambridge University Press

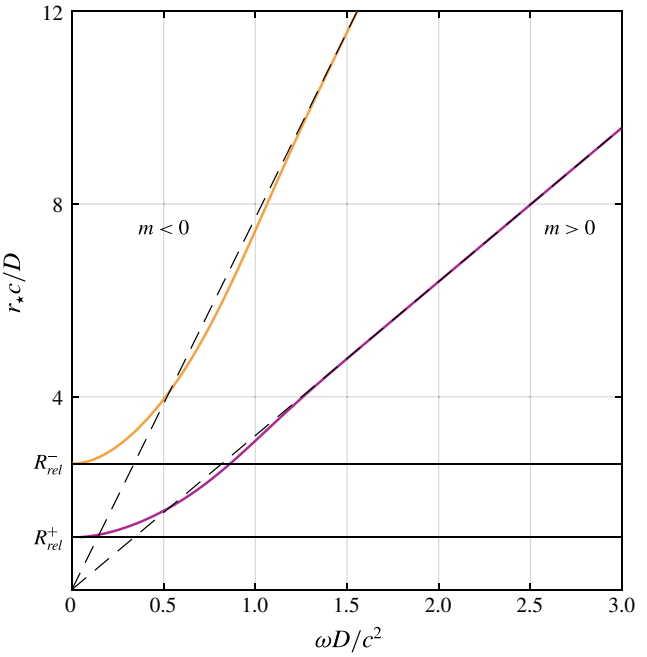



FIGURE 2. (Colour online) Radius of the unstable orbit as a function of the angular frequency of the co- and counter-rotating rays (in purple and orange, respectively) and comparison with the shallow- and deep-water regimes (in solid and dashed black, respectively). We have chosen the flow parameters such that $C/hc = D/hc = 0.9$ (chosen to make the transition from shallow to deep water more visible), where $c = \sqrt{gh}$ is the celerity of shallow-water waves. On the vertical axis, $R^{\pm}_{rel}$ is the value of $r^{\pm}_{\star}$ in the shallow-water (or relativistic) regime. (We recall that, when the frequency varies, the corresponding orbital $m$ also does, so that (4.4) is satisfied.)

Here $k_{in}$ is the incoming wavenumber satisfying the dispersion relation (or the Hamiltonian constraint) at infinity for a given $\omega$ and $v_g^{in}$ is the group velocity at infinity (as the flow is negligible at infinity, the group velocities in the fluid frame and in the laboratory frame are identical). We numerically solve Hamilton's equations (3.4) to find the characteristics. A standard fourth-order Runge–Kutta (RK4) scheme is used. To ensure the validity of our numerical simulation, the step size is chosen such that along the rays the adimensional quantity $|\mathcal{H}/\omega^2|$ is smaller than $10^{-7}$. Our solution therefore satisfies the Hamiltonian constraint. To numerically compute the amplitude of the wave, we use (3.7) with $\nu = 0$. This shows that the flux of wave action is conserved along a tube of rays. Numerically, we use this conservation to obtain the change in amplitude between neighbouring points along two neighbouring rays, by ensuring that the product of the distance between the rays and the wave action is constant. This means that, if the rays converge (diverge), the amplitude will increase (decrease).

Figure 3(*a*) depicts a congruence of rays at fixed angular frequency $\omega = 19.8$ rad s$^{-1}$ impinging on a draining bathtub vortex with parameters $C = 1.6 \times 10^{-2}$ m$^2$ s$^{-1}$, $D = 1 \times 10^{-3}$ m$^2$ s$^{-1}$ and $h = 0.06$ m, corresponding to the laboratory study of Torres *et al.* (2017). We can clearly distinguish two types of rays. The first type are rays that are able to escape to infinity (co-rotating in red and counter-rotating in dashed blue).

https://doi.org/10.1017/jfm.2018.752 Published online by Cambridge University Press

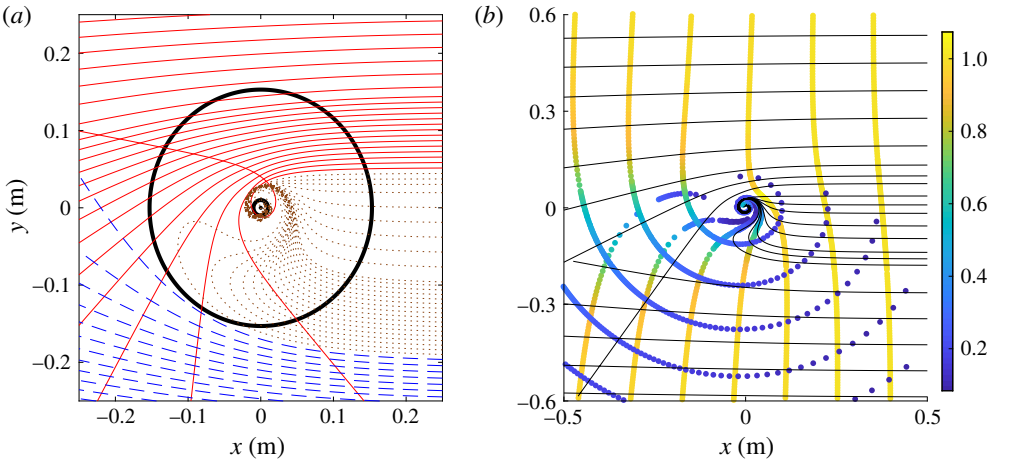



FIGURE 3. (Colour online) (*a*) A congruence of rays incoming from far right on a draining vortex flow. The flow parameters are $C = 1.6 \times 10^{-2}$ m$^2$ s$^{-1}$, $D = 1 \times 10^{-3}$ m$^2$ s$^{-1}$ and $h = 0.06$ m. They correspond to the experimental flow of Torres *et al.* (2017). The angular frequency of the wave is $\omega = 19.8$ rad s$^{-1}$. For these parameters, we have $hk_{in} \simeq 2.4$ and hence are in the deep-water regime. The red (blue) curves represent the co-rotating (counter-rotating) rays escaping to infinity. The dotted brown lines are the rays falling into the hole. The two black circles represent the orbital radius for co- and counter-rotating rays, respectively, at $r = 1$ cm and $r = 15.3$ cm. (*b*) The eikonal wavefront reconstructed from the phase along the rays. The colour scale represents the amplitude of the wave normalized to one initially. The black lines are some rays from (3*a*).

The impact parameter for those rays are beyond some critical values $b_c^{\pm}(\omega)$. We note that $|b_c^-(\omega)| > |b_c^+(\omega)|$, implying that co-rotating rays are able to go closer to the vortex than counter-rotating ones. The second type of rays are those that fall into the vortex core (in dotted brown). We note from (4.15) that the impact parameter depends on the group velocity and therefore on the frequency of the wave. This behaviour differs from the shallow-water regime where the group velocity matches the phase velocity and is constant for all frequency.

In the process of obtaining the rays by solving Hamilton's equations, we also compute the phase of the wave along each trajectory. It is then possible to reconstruct the eikonal wavefronts by finding the constant phase points along each ray (see Dempsey & Dolan (2016) for a shallow-water study). The wavefronts are presented in figure 3(*b*). The coloured dots represent the location of the constant phase points and the colour scale gives the amplitude of the wave at these points. Far from the vortex, where the flow becomes negligible, we can see that the wavefronts are orthogonal to the rays (black lines). On the contrary, closer to the vortex, we clearly observe the non-orthogonality of the wavefronts and the rays where the flow becomes more rapid.

When varying the angular frequency $\omega$, the rays display a similar pattern as in figure 3(*a*), but the orbital radii $r_\star^{\pm}$ vary. When increasing the angular frequency, they interpolate between their shallow-water value to the deep-water behaviour of (4.12). To illustrate this, we plotted the dependence of the orbital radii with the frequency in figure 2.

https://doi.org/10.1017/jfm.2018.752 Published online by Cambridge University Press

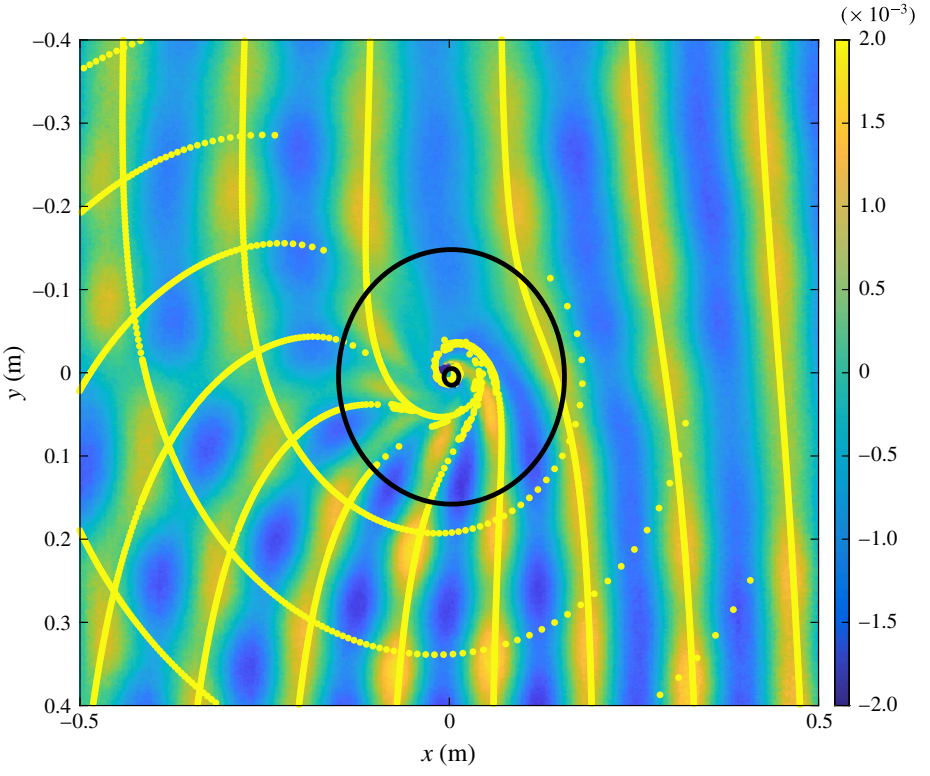



FIGURE 4. (Colour online) Comparison between eikonal wavefront computed numerically and experimental data. The bright yellow dots represent the eikonal wavefront reconstructed from the phase along the rays. The two black circles are the unstable orbits, also present in figure 3(*a*). The background image is a measurement of the free surface of the water. The flow parameters and wave frequency are the same as in figure 3. The frequency of the eikonal wave (3.15 Hz) is chosen so as to obtain the best fit with the 3.27 Hz wave of figure 1 in Torres *et al.* (2017). The two frequencies agree within error bars (approximately 4 %). The colour bar represents the amplitude of the wave in metres.

4.2.1. *Experimental validation*

In figure 4 we compare our ray-tracing results with experimental data taken from the wavetank experiment of Torres *et al.* (2017) with a circulation-to-draining ratio of approximately $C/D \simeq 16$. One can see that, broadly, the eikonal wavefronts agree well with the experiment. We observe small deviations in two regions: close to the centre of the vortex, and after the wave has propagated through the vortex (on the left of the image). The eikonal approximation we used is expected to degrade close to the centre of the vortex, where the flow varies more rapidly. Moreover, cumulative errors might explain the shift between our simulation and the data after the wave has propagated away from the vortex (on the far left side of figure 4).

The good agreement between our numerical solution and the experimental data suggests that circular rays are present in the system (see § 4.1). While the inner one (co-rotating with the vortex) is very close to the centre, in a region where the vortex model of (4.1) becomes questionable, the outer one (counter-rotating) lies in a region where our method provides an accurate description. To estimate the order of the error, we compare the gradient scale of the background to the frequency of the

https://doi.org/10.1017/jfm.2018.752 Published online by Cambridge University Press

wave: $|\partial_r v_\theta|/\omega$. Near the outer light ring $r_\star^+$, this ratio reduces to the inverse of the azimuthal number $m_\star$ and is approximately 0.1. As a last remark, we point out that, within our approximation, the locations of the rays are usually more accurate than the phase itself. This is because the phase is rapidly varying, but the local momentum is slowly varying (see the discussion in § 4.3.4 of Bühler (2014)). Hence, this fact and the good agreement in figure 4 strengthen our conclusion regarding the presence of circular orbits around the vortex of figure 4.

## 5. Characteristic damped resonances of a draining vortex: the quasi-normal mode spectrum

We anticipate that the presence of 'rings' (i.e. circular rays/characteristics) in the vortex system will influence the time-dependent response to a small wave excitation, through certain characteristic damped oscillations. In the black hole case, the time-dependent response of a black hole to a perturbation typically bears the imprint of one or more quasi-normal modes (QNMs) (Berti *et al.* 2009). The QNMs are a discrete set of modes with complex frequencies, with the real part determining the oscillation frequency, and the (negative) imaginary part determining the damping rate. Formally, QNMs are defined via a pair of boundary conditions to be those modes which are ingoing at the horizon and outgoing far from the black hole. In the eikonal limit, one finds that the spectrum is governed chiefly by the properties of the circular orbits (see e.g. Cardoso *et al.* 2009). More precisely, the eikonal complex frequencies are given by

$$\omega_{QNM}(m) = \omega_\star(m) - \mathrm{i}\Lambda(m)(n + \tfrac{1}{2}), \tag{5.1}$$

where $\omega_\star(m)$ is the circular orbit wave frequency of § 4.1, $n$ is an integer called the overtone index, and $\Lambda$ is the decay rate of these (unstable) orbits (Lyapunov exponent), to be defined below.

The notion of QNMs extends to many different contexts. QNMs typically arise in open systems, or systems with leakage (in our case, the drain plays that role). As we shall see, around a draining vortex, surface wave decay is also driven by a discrete set of complex frequencies, which can be obtained approximately using the structure of circular orbits.

Owing to the presence of circular orbits, we expect that, if one perturbs the system initially, the perturbations will spread out rapidly, except where the perturbation lingers around the circular orbit. Indeed, a wave packet passing close to such a 'ring' can hover around it for a longer time before dispersing. To understand this behaviour more precisely, we consider a wave packet in the neighbourhood of a circular orbit, that is, around the family of rays $(r_\star + \delta r,\ \ k_{r\star} + \delta k,\ \ \omega_\star + \delta\omega)$ at a fixed azimuthal number $m$. To obtain the effective dynamics of these rays, we expand the Hamiltonian in the vicinity of the critical point $(r_\star, k_{r\star})$. This gives

$$\mathcal{H} = \partial_\omega \mathcal{H}\, \delta\omega + \tfrac{1}{2}\boldsymbol{X}^{\mathrm{T}} \cdot [\mathrm{d}^2\mathcal{H}] \cdot \boldsymbol{X}, \tag{5.2}$$

where we have defined the Hessian matrix

$$[\mathrm{d}^2\mathcal{H}] = \begin{pmatrix} \partial_k^2\mathcal{H} & \partial_k\partial_r\mathcal{H} \\ \partial_k\partial_r\mathcal{H} & \partial_r^2\mathcal{H} \end{pmatrix} \quad \text{and} \quad \boldsymbol{X} = \begin{pmatrix} \delta k \\ \delta r \end{pmatrix}. \tag{5.3a,b}$$

Since $[\mathrm{d}^2\mathcal{H}]$ is a symmetric and real matrix, it can be diagonalized. We call $(\mu_1, \mu_2)$ the eigenvalues, and $(R, K)$ the components in the eigenbasis. (In addition, the

https://doi.org/10.1017/jfm.2018.752 Published online by Cambridge University Press

eigenbasis is orthogonal, which in two dimensions is enough to ensure a canonical transformation $(\delta r, \delta k) \to (R, K)$.) In this representation, the Hamiltonian becomes

$$\mathcal{H} = \partial_\omega \mathcal{H} \delta\omega + \tfrac{1}{2}\mu_1 K^2 + \tfrac{1}{2}\mu_2 R^2. \tag{5.4}$$

This is the Hamiltonian of a harmonic oscillator. The relative sign of the coefficients $\mu_1$ and $\mu_2$ will determine the stability of the orbits. In our case, we always have $\mu_1\mu_2 < 0$ and hence the orbit is unstable. In its vicinity, wave dynamics is described by an inverted harmonic oscillator. To obtain the Lyapunov exponent $\Lambda$, we solve Hamilton's equations with this reduced Hamiltonian. This gives

$$\dot{R} = \mu_1 K, \quad \dot{K} = -\mu_2 R, \quad \dot{t} = -\partial_\omega \mathcal{H}. \tag{5.5a–c}$$

The general solution is a linear superposition of decaying and growing exponentials. At late times, the growing behaviour dominates, and we have

$$R \sim A\mathrm{e}^{(\sqrt{-\mu_1\mu_2}/\partial_\omega \mathcal{H})t} \quad \text{and} \quad K \sim B\mathrm{e}^{(\sqrt{-\mu_1\mu_2}/\partial_\omega \mathcal{H})t}, \tag{5.6a,b}$$

where $A$ and $B$ are constant coefficients such that (5.5) is satisfied. The Lyapunov exponent is the rate of exponential growth away from the orbit, and is given by

$$\Lambda = \frac{\sqrt{-\mu_1\mu_2}}{|\partial_\omega \mathcal{H}|} = \frac{\sqrt{-\det[\mathrm{d}^2\mathcal{H}]}}{|\partial_\omega \mathcal{H}|}. \tag{5.7}$$

The Lyapunov exponent governs the decay of waves close to the circular orbit. One can see this by inspecting the amplitude governed by the transport equation (3.7), namely,

$$A_0(t) \propto \mathrm{e}^{-\Lambda t/2}. \tag{5.8}$$

However, this argument misses the overtone frequencies (i.e. $n \neq 0$ in (5.1)).

A more precise argument is to lift the reduced Hamiltonian (5.4) at the level of the wave equation. To see this, we consider a wave packet of fixed $m$, localized around the circular orbit, written as

$$\phi(t, r_\star + \delta r) \sim \psi(t, \delta r)\mathrm{e}^{-\mathrm{i}\omega_\star t + \mathrm{i}k_{r_\star} r}, \tag{5.9}$$

where $\psi$ is a slowly varying envelope. Formally, the wave equation (2.1) can be written as

$$\hat{\mathcal{H}}(\omega = \mathrm{i}\partial_t;\, r,\, k_r = -\mathrm{i}\partial_r)\phi = 0. \tag{5.10}$$

(This writing is, of course, only formal, since there is *a priori* no unique way to promote the Hamiltonian function $\mathcal{H}(\omega, r, k_r)$ into an operator $\hat{\mathcal{H}}(\mathrm{i}\partial_t; r, -\mathrm{i}\partial_r)$. The ambiguities essentially come from the various possible orderings between functions of $r$ and $\partial_r$. However, since we work here at the level of the eikonal approximation, different choices of ordering lead to the same result.) Assuming $\psi$ in (5.9) is slowly varying, one can again rescale $\partial \to \epsilon\partial$ and expand in $\epsilon$. Doing so, the effective wave equation in the vicinity of the circular orbit is given by

$$-\mathrm{i}\partial_\omega \mathcal{H}\partial_t\psi = -\tfrac{1}{2}\partial_k^2\mathcal{H}\partial_r^2\psi - \tfrac{1}{2}\mathrm{i}\partial_k\partial_r\mathcal{H}(r\partial_r + \partial_r r)\psi + \tfrac{1}{2}\partial_r^2\mathcal{H}r^2\psi. \tag{5.11}$$

https://doi.org/10.1017/jfm.2018.752 Published online by Cambridge University Press

(Note that the cross-term is chosen to be symmetric.) This equation is a Schrödinger equation in an upside-down harmonic potential. To see this, we use the fact that there is a canonical transformation to diagonalize the Hamiltonian (5.2). At the level of the Schrödinger equation (5.11), this means that there is a unitary transformation $\psi \to \tilde{\psi}$ such that

$$-\mathrm{i}\partial_\omega \mathcal{H} \partial_t \tilde{\psi} = -\tfrac{1}{2}\mu_1 \partial_R^2 \tilde{\psi} + \tfrac{1}{2}\mu_2 R^2 \tilde{\psi}. \tag{5.12}$$

In the case of (5.12) the time-dependent response is well described with the help of quasi-normal modes, defined as the solutions of $\mathrm{i}\partial_t \tilde{\psi} = \delta\omega \tilde{\psi}$ with purely outgoing boundary conditions (see e.g. Kokkotas & Schmidt 1999). Such solutions are analytically known, and can be expressed using parametric cylinder functions. This selects a discrete set of complex values for $\delta\omega$, which are the quasi-normal frequencies for $\tilde{\psi}$ and hence for $\psi$. Finally, using (5.9), we see that the quasi-normal frequencies for $\phi$ are given by (5.1).

Alternative boundary conditions, such as those for exotic black hole mimickers, can alter the global structure of the quasi-normal mode spectrum, without significantly altering the local 'ringing' phenomena associated with the light ring (see e.g. Cardoso & Pani 2017*a*,*b*).

We have numerically computed the fundamental ($n = 0$) eikonal quasi-normal frequencies in the full dispersive regime for a selection of azimuthal numbers and for several values of the ratio $C/D$. The result and the comparison with the linear regime are presented in figure 5. We can see that the behaviour of the counter-rotating modes ($m < 0$) is very similar in the two different regimes. As the ratio increases, the radius of the unstable orbits of these modes will increase too. For fixed $m$, the increase of the radius will increase the wavelength (decrease the frequency) and therefore will bring the mode closer to the linear regime. On the other side, the behaviour for co-rotating ($m > 0$) modes is very different when dispersion is included. Indeed, in the relativistic regime, the lifetime of the co-rotating modes decreases while it appears to increase after a short drop as an effect of dispersion.

In general, it is noticeable that the co-rotating modes are damped quicker than the counter-rotating ones (see figure 5). Hence, if the initial excitation has a similar amplitude on both radii, the dominant signal at large time will be that of the counter-rotating orbit. This is the case, for instance, if the system is excited by sending a plane wave, which contains as much $m > 0$ as $m < 0$ (as in figure 4). In addition, we expect the counter-rotating mode to have a larger spatial extension than the co-rotating one since the radius of the counter-rotating orbit is larger that the co-rotating one, and hence will be more visible.

## 6. Discussion

It is known that waves in a shallow potential flow are governed, approximately, by a wave equation equivalent to that governing a scalar field on an effective spacetime. By means of this analogy, peculiar and fundamental effects that were before out of reach are now observable in the laboratory. Recent water-wave experiments with draining, circulating flows have found that one of these analogue phenomena, namely black hole superradiance, persists beyond the shallow regime, where dispersive and dissipative effects render incomplete the spacetime description of the system. In this work, we have applied a ray-tracing (gradient expansion) method to a realistic dispersive, dissipative wave equation. We argued that fundamental features of vortex

https://doi.org/10.1017/jfm.2018.752 Published online by Cambridge University Press

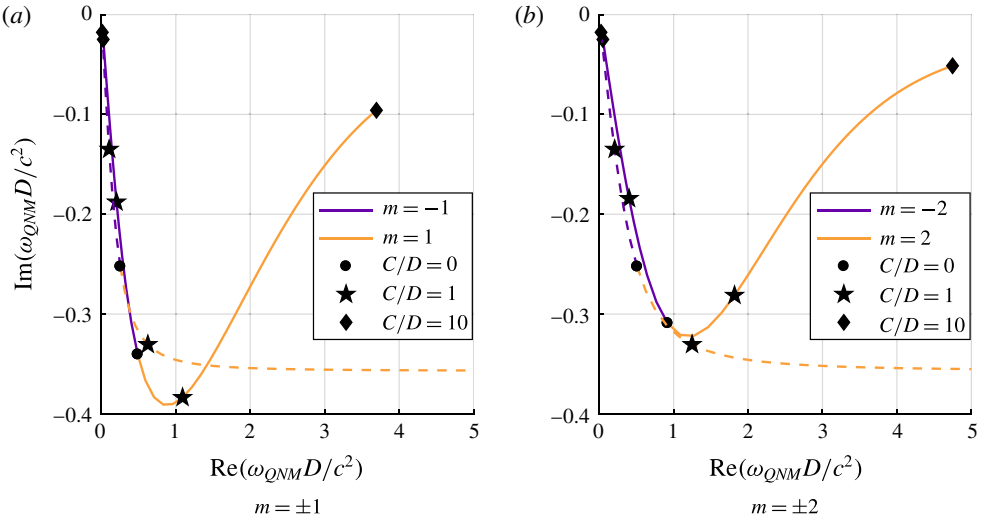



FIGURE 5. (Colour online) Fundamental quasi-normal mode frequencies $\omega_{QNM}$ of different $m$ modes, $m=\pm1$ (*a*) and $m=\pm2$ (*b*), for various ratios $C/D$. The dashed line is the shallow-water result, and the solid one the (general) dispersive regime. In order to make the transition more transparent, the depth is chosen so that $gh^3/D^2=0.04$. Each point represents a different ratio for the flow parameters. The negative $m$ modes have a similar behaviour in the two regimes, namely their lifetime increases as the ratio $C/D$ increases. On the other hand, the lifetime of the positive $m$ modes increases too with the ratio $C/D$ in the dispersive regime while it monotonically decrease in the absence of dispersion.

wave scattering can be understood with reference to a pair of (frequency-dependent) circular rays (rings), which are analogous to the light rings of black holes.

In addition, we have reconstructed the wavefronts of a plane wave scattering on a vortex using the ray-tracing approximation. This allows us to test our methods against the experimental results of Torres *et al.* (2017) (see figure 4). The agreement with the data suggests the presence of an outer light ring (for counter-rotating modes) and raises the challenge of observing it. This could be done through the observation of quasi-normal modes of the vortex flow that are a generic consequence of light rings. We discussed these quasi-normal modes and their relation to circular orbits in § 5. In particular we have shown that the effect of dispersion on the counter-rotating modes will be the most important when the drain predominates over the circulation. This is the case in the experiment of Torres *et al.* (2017), where the ratio $C/D\simeq16$. Another interesting feature of dispersion is that the lifetime of the QNM increases at high circulation. For the co-rotating mode, this behaviour significantly differs from the non-dispersive (shallow-water) regime and might lead to an instability if the decay of those modes becomes smaller than their amplification via superradiance (Hod 2014; Oliveira, Cardoso & Crispino 2014; Brito *et al.* 2015). As a last remark, we would like to point out that these phenomena may also be relevant on oceanic scales; for instance Haller & Beron-Vera (2013) have shown the presence of similar analogue black hole light rings in the South Atlantic portion of the Atlantic Ocean.

**Acknowledgements**

We want to thank S. Patrick and Z. Fifer for the many useful discussions at various stages of the project. We also thank T. Napier and T. Wright for their help

https://doi.org/10.1017/jfm.2018.752 Published online by Cambridge University Press

and guidance with the experimental set-up. S.D. thanks D. Dempsey for helpful discussions. This project has received funding from the European Union's Horizon 2020 research and innovation programme under the Marie Skłodowska-Curie grant agreement no. 655524. S.W. acknowledges financial support provided under the Royal Society University Research Fellow (UF120112), the Nottingham Advanced Research Fellow (A2RHS2) and the Royal Society project (RG130377) grants, and the Engineering and Physical Sciences Research Council (EPSRC) project grant (EP/P00637X/1). S.W. acknowledge partial support from Science and Technology Facilities Council (STFC) consolidated grant no. ST/P000703/. S.D. acknowledges financial support from the EPSRC under grant no. EP/M025802/1, from the STFC under grant no. ST/L000520/1 and the project H2020-MSCA-RISE-2017 grant FunFiCO-777740.

## Appendix A. General method of ray tracing

In this appendix we review the general framework for solving (2.1) using a gradient expansion (see e.g. Bühler 2014). To do so, we consider the rescaling of (2.1) as follows:

$$\partial \to \epsilon \partial, \tag{A 1a}$$

$$\nu \to \epsilon \nu. \tag{A 1b}$$

The second line translates the fact that we consider dissipation to be weak – over a scale of the order of the gradient scale (it is also more natural to impose a real-valued Hamilton–Jacobi equation (3.2), which imposes the need to include dissipation in the amplitude equation). As in the text, we assume a solution to the wave equation of the form

$$\phi = A \exp\left(\mathrm{i}\frac{S}{\epsilon}\right), \tag{A 2}$$

where $\phi$, $A$ and $S$ are functions of $\boldsymbol{x}$ and $t$; and $A$ and $S$ can be expanded as power series in the small parameter $\epsilon$:

$$S = \sum_{n=0}^{+\infty} \epsilon^n S_n \quad \text{and} \quad A = \sum_{n=0}^{+\infty} \epsilon^n A_n. \tag{A 3a,b}$$

The role of $\epsilon$ is to keep track of the hierarchy of terms in the gradient expansion. Intuitively, it can be seen as the ratio between the gradient scale and the wavelength. We now seek the leading-order equations for both $S$ and $A$. The obtained solutions give us approximate wave solutions using (3.1) that we shall refer to as eikonal waves.

### A.1. *Ray-tracing equations*

We start from the wave equation (2.1) with the ansatz (3.1) for $\phi$ and keep only the leading-order term in $\epsilon$. To do so, we expand the function $F$ as a Taylor expansion:

$$F(-\mathrm{i}\epsilon\nabla) = \sum_{n=1}^{+\infty} T_{2n}(-1)^n \epsilon^{2n} \Delta^n, \tag{A 4}$$

https://doi.org/10.1017/jfm.2018.752 Published online by Cambridge University Press

where $\Delta \equiv \nabla^2 = \partial_x^2 + \partial_y^2$ is the two-dimensional Laplacian. To expand the term $F(-\mathrm{i}\boldsymbol{\nabla})\phi$ of (2.1), we look at each term of the Taylor series (A 4) separately. Using the binomial formula, we obtain

$$\begin{aligned}\Delta^n\phi &= \sum_{k=0}^{n}\binom{n}{k}\partial_x^{2k}\partial_y^{2n-2k}\phi,\\ &\simeq \frac{(-1)^n}{\epsilon^{2n}}\sum_{k=0}^{n}\binom{n}{k}(\partial_x S_0)^{2k}(\partial_y S_0)^{2n-2k}A\mathrm{e}^{\mathrm{i}S_0/\epsilon},\\ &\simeq \frac{(-1)^n}{\epsilon^{2n}}((\partial_x S_0)^2+(\partial_y S_0)^2)^n A\mathrm{e}^{\mathrm{i}S_0/\epsilon},\end{aligned} \tag{A 5}$$

where $\simeq$ means that we have kept only the leading term in $\epsilon$. Re-summing the Taylor series (A 4), we see that

$$F(-\mathrm{i}\epsilon\boldsymbol{\nabla})\phi \simeq A\mathrm{e}^{\mathrm{i}S_0/\epsilon}F(\boldsymbol{\nabla}S_0). \tag{A 6}$$

The same applies for the material derivative, that is

$$\mathcal{D}_t^2\phi \simeq -A\mathrm{e}^{\mathrm{i}S/\epsilon}(\mathcal{D}_t S_0)^2. \tag{A 7}$$

Combining (A 6) and (A 7), it follows that, at leading order, the phase $S_0$ obeys the Hamilton–Jacobi equation (3.2).

### A.2. *Transport equation*

Above, we derived the ray equations from the leading-order-in-$\epsilon$ term of the wave equation. We now focus on the next-to-leading-order term, and show that it leads to a transport equation for the amplitude of the wave. Let us first examine the next-to-leading-order term of the action of $\mathcal{D}_t^2$ on $\phi$. As $\mathcal{D}_t^2$ contains two derivatives, the next-to-leading-order term of its action on $\phi$ is attained when only one derivative hits the exponential,

$$\mathcal{D}_t^2\phi \simeq \frac{-\mathrm{i}\epsilon}{A_0}\mathcal{D}_t(A_0^2\Omega_0), \tag{A 8}$$

where we have introduced $\Omega_0 = \omega - \boldsymbol{v}_0\cdot\boldsymbol{\nabla}S_0$ the comoving angular frequency of the wave. We get the action of the operator $F(-\mathrm{i}\epsilon\boldsymbol{\nabla})$ the same way. To obtain the next-to-leading-order term of $\Delta^n\phi$ (in $1/\epsilon^{2n-1}$), we must count the number of terms in the expansion of (A 5) such that the exponential $\mathrm{e}^{\mathrm{i}S/\epsilon}$ is derived exactly $2n-1$ times. The last derivative of $\Delta^n$ will then act on $A_0$ or $\boldsymbol{\nabla}S_0$. Doing so, we obtain

$$\Delta^n\phi \simeq \frac{(-1)^{n-1}}{\epsilon^{2n-1}}\mathrm{i}\left(2n\boldsymbol{\nabla}A_0\cdot(\boldsymbol{\nabla}S_0)^{2n-1}+\frac{2n(2n-1)}{2}A_0\cdot(\boldsymbol{\nabla}S_0)^{2n-2}\Delta S_0\right)\mathrm{e}^{\mathrm{i}S/\epsilon}. \tag{A 9}$$

Re-summing the Taylor series, we recognize the derivative with respect to the momenta of the function $F$. Gathering the terms, the action of $F(-\mathrm{i}\epsilon\boldsymbol{\nabla})$ can be rewritten as a total derivative:

$$F(-\mathrm{i}\epsilon\boldsymbol{\nabla})A_0\mathrm{e}^{\mathrm{i}S/\epsilon} \simeq -\frac{\mathrm{i}\epsilon}{2A_0}\boldsymbol{\nabla}\cdot(A_0^2\boldsymbol{\nabla}_k F(\boldsymbol{\nabla}S_0)). \tag{A 10}$$

Finally, a similar calculation yields the action of the damping operator,

$$2\epsilon\nu\gamma(-\mathrm{i}\boldsymbol{\nabla})\mathcal{D}_t\phi \simeq 2\mathrm{i}\epsilon\nu\Omega_0 A_0\gamma(\boldsymbol{\nabla}S_0). \tag{A 11}$$

Combining the action of the three operators, we obtain the equation for the amplitude used in the text, i.e. equation (3.7).

https://doi.org/10.1017/jfm.2018.752 Published online by Cambridge University Press

## Appendix B. Orbits in the deep-water regime

We detail here the derivation of (4.12). As we have seen, there are two different light rings (represented by the $\pm$ in (4.7)). In order to keep track of this sign, we introduce $\epsilon_m = \mathrm{sign}(m)$. Using it, we can express $m$ as a function of $r$ as

$$m = \epsilon_m \frac{g r_\star^3}{4B_\pm^2}\sqrt{1-\frac{D^2}{B_\pm^2}}. \tag{B 1}$$

We shall also use the parameters $B_\pm$ introduced in (4.8). On a circular orbit, we can use the Hamiltonian constraint to express the orbital frequency in terms of the other parameters:

$$\omega_\star = -\frac{D}{r_\star}k_{r\star} + \frac{C}{r_\star}\frac{m}{r_\star} + \sqrt{gk}. \tag{B 2}$$

Substituting (4.10) and (4.11) in the above equation, we obtain

$$\omega_\star = \frac{g r_\star}{2B_\pm}\left(-\frac{D^2}{2B_\pm^2} + \epsilon_m \frac{C}{2B_\pm^2}\sqrt{B^2-D^2}+1\right). \tag{B 3}$$

We now rewrite our flow parameters $C$ and $D$ as

$$C = R\sin(\phi) \quad \text{and} \quad D = R\cos(\phi), \tag{B 4a,b}$$

and $B_\pm$ becomes

$$B = \sqrt{2}R\sqrt{1-\epsilon_m \sin(\phi)}. \tag{B 5}$$

Inserting (B 4) and (B 5) into (B 3) we get

$$\omega_\star = \frac{g r_\star}{8B_\pm}\left(-\frac{\cos^2(\phi)}{1-\epsilon_m\sin(\phi)} + \epsilon_m \frac{\sin(\phi)\sqrt{2-2\epsilon_m\sin(\phi)-\cos^2(\phi)}}{1-\epsilon_m\sin(\phi)} + 4\right). \tag{B 6}$$

Using $\cos^2(\phi) = 1-\sin^2(\phi)$, we can simplify this expression to

$$\omega_\star = \frac{g r_\star}{8B_\pm}\left(\frac{-1+\sin^2(\phi)}{1-\epsilon_m\sin(\phi)} + \epsilon_m\sin(\phi) + 4\right), \tag{B 7}$$

which further simplifies into

$$\omega_\star = \frac{3 g r_\star}{8B_\pm}. \tag{B 8}$$

We can inverse this relation to obtain $r_\star$ as a function of $\omega_\star$ or express $r_\star$ in terms of $m$ to obtain the effective dispersion relation (4.13).

https://doi.org/10.1017/jfm.2018.752 Published online by Cambridge University Press

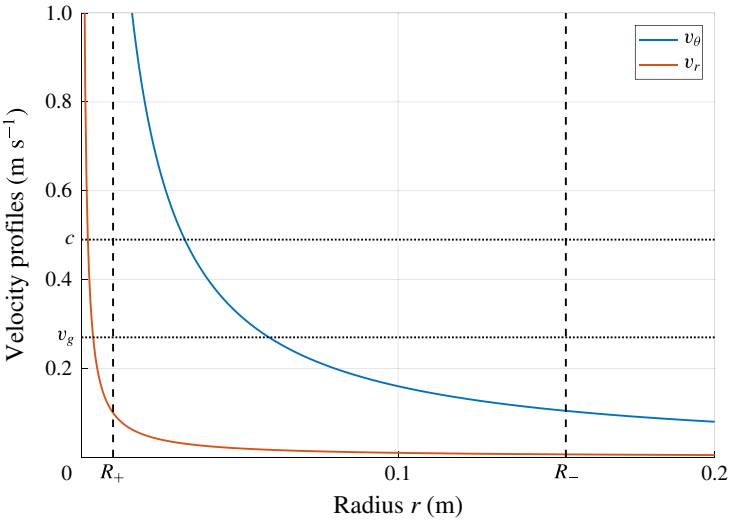



FIGURE 6. (Colour online) Radial (in red) and angular (in blue) velocity profiles as functions of the radius $r$. The profiles are plotted for $C = 1.6 \times 10^{-2}$ m$^2$ s$^{-1}$ and $D = 1 \times 10^{-3}$ m$^2$ s$^{-1}$. The dashed vertical black lines represent the values of the two circular orbit radii. The dotted horizontal black lines depict the value of the group velocity and phase velocity of the wave for the frequency considered in figure 3 (3.15 Hz). As the radial velocity is much smaller than the angular one, the total velocity is approximately equal to the angular one and it matches the group velocity of the waves at approximately 7 cm.

## Appendix C. Velocity profiles

Here in figure 6 we present the velocity profiles used in our model in order to compare the various quantities entering into our discussion.

## REFERENCES

ABBOTT, B. P. *et al.* 2016 Observation of gravitational waves from a binary black hole merger. *Phys. Rev. Lett.* **116**, 061102.

ACHESON, D. J. 1976 On over-reflexion. *J. Fluid Mech.* **77** (3), 433–472.

BARCELO, C., LIBERATI, S. & VISSER, M. 2005 Analogue gravity. *Living Rev. Rel.* **8**, 12 (revised as *Living Rev. Rel.* **14** (3), (2011)).

BERRY, M. V., CHAMBERS, R. G., LARGE, M. D., UPSTILL, C. & WALMSLEY, J. C. 1980 Wavefront dislocations in the Aharonov–Bohm effect and its water wave analogue. *Eur. J. Phys.* **1** (3), 154–162.

BERTI, E., CARDOSO, V. & STARINETS, A. O. 2009 Quasinormal modes of black holes and black branes. *Class. Quant. Grav.* **26**, 163001.

BRITO, R., CARDOSO, V. & PANI, P. 2015 *Superradiance*, Lecture Notes in Physics, 906, pp. 1–237. Springer.

BÜHLER, O. 2014 *Waves and Mean Flows*. Cambridge University Press.

BÜHLER, O. & MCINTYRE, M. 2005 Wave capture and wave vortex duality. *J. Fluid Mech.* **534**, 67–95.

CARDOSO, V., MIRANDA, A. S., BERTI, E., WITEK, H. & ZANCHIN, V. T. 2009 Geodesic stability, Lyapunov exponents, and quasinormal modes. *Phys. Rev.* D **79**, 064016.

https://doi.org/10.1017/jfm.2018.752 Published online by Cambridge University Press

CARDOSO, V. & PANI, P. 2017*a* Tests for the existence of black holes through gravitational wave echoes. *Nat. Astron.* **1** (9), 586–591.

CARDOSO, V. & PANI, P. 2017*b* Tests for the existence of black holes through gravitational wave echoes. *Nat. Astron.* **1**, 586–591.

CERDA, E. & LUND, F. 1993 Interaction of surface waves with vorticity in shallow water. *Phys. Rev. Lett.* **70** (25), 3896.

COSTE, C. & LUND, F. 1999 Scattering of dislocated wave fronts by vertical vorticity and the Aharonov–Bohm effect. II. Dispersive waves. *Phys. Rev.* E **60** (4), 4917.

COSTE, C., LUND, F. & UMEKI, M. 1999 Scattering of dislocated wave fronts by vertical vorticity and the Aharonov–Bohm effect. I. Shallow water. *Phys. Rev.* E **60** (4), 4908.

DECANINI, Y., ESPOSITO-FARESE, G. & FOLACCI, A. 2011 Universality of high-energy absorption cross sections for black holes. *Phys. Rev.* D **83**, 044032.

DEMPSEY, D. 2017 Wave propagation on black hole spacetimes. PhD thesis, School of Mathematics and Statistics, University of Sheffield.

DEMPSEY, D. & DOLAN, S. R. 2016 Waves and null congruences in a draining bathtub. *Intl J. Mod. Phys.* D **25** (9), 1641004.

DOLAN, S. R. 2010 Quasinormal mode spectrum of a Kerr black hole in the eikonal limit. *Phys. Rev.* D **82**, 104003.

DOLAN, S. R., OLIVEIRA, E. S. & CRISPINO, L. C. B. 2011 Aharonov–Bohm effect in a draining bathtub vortex. *Phys. Lett.* B **701** (4), 485–489.

DOLAN, S. R., OLIVEIRA, L. A. & CRISPINO, L. C. B. 2012 Resonances of a rotating black hole analogue. *Phys. Rev.* D **85**, 044031.

DOLAN, S. R. & STRATTON, T. 2017 Rainbow scattering in the gravitational field of a compact object. *Phys. Rev.* D **95** (12), 124055.

EUVÉ, L. P., MICHEL, F., PARENTANI, R., PHILBIN, T. G. & ROUSSEAUX, G. 2016 Observation of noise correlated by the Hawking effect in a water tank. *Phys. Rev. Lett.* **117** (12), 121301.

FABRIKANT, A. L. & RAEVSKY, M. A. 1994 The influence of drift flow turbulence on surface gravity wave propagation. *J. Fluid Mech.* **262**, 141–156.

FETTER, A. L. 1964 Scattering of sound by a classical vortex. *Phys. Rev.* **136** (6A), A1488.

GOEBEL, C. J. 1972 Comments on the 'vibrations' of a black hole. *Astrophys. J.* **172**, L95.

HALLER, G. & BERON-VERA, F. J. 2013 Coherent Lagrangian vortices: the black holes of turbulence. *J. Fluid Mech.* **731**, R4.

HOD, S. 2014 Onset of superradiant instabilities in the composed Kerr-black-hole-mirror bomb. *Phys. Lett.* B **736**, 398–402.

HUNT, J. N. 1964 The viscous damping of gravity waves in shallow water. *La Houille Blanche* **6**, 685–691.

JACOBSON, T. 2013 Black holes and Hawking radiation in spacetime and its analogues. Lecture Notes in Physics, 870, pp. 1–29. Springer.

JANSSON, T. R. N., HASPANG, M. P., JENSEN, K. H., HERSEN, P. & BOHR, T. 2006 Polygons on a rotating fluid surface. *Phys. Rev. Lett.* **96** (17), 174502.

KOKKOTAS, K. D. & SCHMIDT, B. G. 1999 Quasinormal modes of stars and black holes. *Living Rev. Rel.* **2**, 2.

KONOPLYA, R. A. & STUCHLÍK, Z. 2017 Are eikonal quasinormal modes linked to the unstable circular null geodesics? *Phys. Lett.* B **771**, 597–602.

KOPIEV, V. F. & BELYAEV, I. V. 2010 On long-wave sound scattering by a Rankine vortex: non-resonant and resonant cases. *J. Sound Vib.* **329** (9), 1409–1421.

LUND, F. & ROJAS, C. 1989 Ultrasound as a probe of turbulence. *Physica* D **37** (1–3), 508–514.

MACEDO, C. F. B., LEITE, L. C. S., OLIVEIRA, E. S., DOLAN, S. R. & CRISPINO, L. C. B. 2013 Absorption of planar massless scalar waves by Kerr black holes. *Phys. Rev.* D **88** (6), 064033.

MATZNER, R. A., DEWITTE-MORETTE, C., NELSON, B. & ZHANG, T.-R. 1985 Glory scattering by black holes. *Phys. Rev.* D **31** (8), 1869.

MILEWSKI, P. A. & KELLER, J. B. 1996 Three-dimensional water waves. *Stud. Appl. Maths* **97** (2), 149–166.

https://doi.org/10.1017/jfm.2018.752 Published online by Cambridge University Press

MOREIRA, R. M. & PEREGRINE, D. H. 2012 Nonlinear interactions between deep-water waves and currents. *J. Fluid Mech.* **691**, 1–25.

MOUGEL, J., FABRE, D., LACAZE, L. & BOHR, T. 2017 On the instabilities of a potential vortex with a free surface. *J. Fluid Mech.* **824**, 230–264.

NAZARENKO, S. V. 1994 Absorption of sound by vortex filaments. *Phys. Rev. Lett.* **73** (13), 1793.

NAZARENKO, S. V., ZABUSKY, N. J. & SCHEIDEGGER, T. 1995 Nonlinear sound–vortex interactions in an inviscid isentropic fluid: a two-fluid model. *Phys. Fluids* **7** (10), 2407–2419.

OLIVEIRA, L. A., CARDOSO, V. & CRISPINO, L. C. B. 2014 Ergoregion instability: the hydrodynamic vortex. *Phys. Rev.* D **89** (12), 124008.

PAGNEUX, V. & MAUREL, A. 2001 Irregular scattering of acoustic rays by vortices. *Phys. Rev. Lett.* **86** (7), 1199.

PRZADKA, A., CABANE, B., PAGNEUX, V., MAUREL, A. & PETITJEANS, P. 2012 Fourier transform profilometry for water waves: how to achieve clean water attenuation with diffusive reflection at the water surface? *Exp. Fluids* **52** (2), 519–527.

ROBERTSON, S. & ROUSSEAUX, G. 2017 Viscous dissipation of surface waves and its relevance to analogue gravity experiments, arXiv:1706.05255.

SCHUTZ, B. F. & WILL, C. M. 1985 Black hole normal modes – a semianalytic approach. *Astrophys. J.* **291**, L33–L36.

SCHÜTZHOLD, R. & UNRUH, W. G. 2002 Gravity wave analogues of black holes. *Phys. Rev.* D **66**, 044019.

SONIN, E. 2002 Magnus force and Aharonov–Bohm effect in superfluids. In *Vortices in Unconventional Superconductors and Superfluids*, pp. 119–145. Springer.

STEINHAUER, J. 2016 Observation of quantum Hawking radiation and its entanglement in an analogue black hole. *Nat. Phys.* **12**, 959.

STOKES, T. E., HOCKING, G. C. & FORBES, L. K. 2008 Unsteady free surface flow induced by a line sink in a fluid of finite depth. *Comput. Fluids* **37** (3), 236–249.

TOPHØJ, L., MOUGEL, J., BOHR, T. & FABRE, D. 2013 Rotating polygon instability of a swirling free surface flow. *Phys. Rev. Lett.* **110** (19), 194502.

TORRES, T., PATRICK, S., COUTANT, A., RICHARTZ, M., TEDFORD, E. W. & WEINFURTNER, S. 2017 Observation of superradiance in a vortex flow. *Nat. Phys.* **13**, 833–836.

UMEKI, M. & LUND, F. 1997 Spirals and dislocations in wave–vortex systems. *Fluid Dyn. Res.* **21** (3), 201–210.

UNRUH, W. G. 1981 Experimental black hole evaporation. *Phys. Rev. Lett.* **46**, 1351–1353.

VANDEN-BROECK, J.-M. & KELLER, J. B. 1987 Free surface flow due to a sink. *J. Fluid Mech.* **175**, 109–117.

VATISTAS, G. H., WANG, J. & LIN, S. 1994 Recent findings on Kelvin's equilibria. *Acta Mechanica* **103** (1–4), 89–102.

VISSER, M. 1998 Acoustic black holes: horizons, ergospheres, and Hawking radiation. *Class. Quant. Grav.* **15**, 1767–1791.

VIVANCO, F., CABALLERO, L., MELO, F. & LUND, F. 2000 Surface waves scattering by a vertical vortex: a progress report. In *Instabilities and Nonequilibrium Structures VI*, pp. 219–231. Springer.

VIVANCO, F., MELO, F., COSTE, C. & LUND, F. 1999 Surface wave scattering by a vertical vortex and the symmetry of the Aharonov–Bohm wave function. *Phys. Rev. Lett.* **83** (10), 1966.

VOCKE, D., MAITLAND, C., PRAIN, A., BIANCALANA, F., MARINO, F. & FACCIO, D. 2017 Rotating black hole geometries in a two-dimensional photon superfluid, arXiv:1709.04293.

WEINFURTNER, S., TEDFORD, E. W., PENRICE, M. C. J., UNRUH, W. G. & LAWRENCE, G. A. 2011 Measurement of stimulated hawking emission in an analogue system. *Phys. Rev. Lett.* **106**, 021302.

YANG, H., NICHOLS, D. A., ZHANG, F., ZIMMERMAN, A., ZHANG, Z. & CHEN, Y. 2012 Quasinormal-mode spectrum of Kerr black holes and its geometric interpretation. *Phys. Rev.* D **86**, 104006.

https://doi.org/10.1017/jfm.2018.752 Published online by Cambridge University Press